



Structural, mechanical, electronic, and anisotropic properties of niobium-doped strontium ferrite: first-principle calculations

Md. Zahid Hasan¹ · Khandaker Monower Hossain² · S. K. Mitro³ · Md. Rasheduzzaman¹ · Jibon Krishna Modak⁴ · M. A. Rayhan⁵

Received: 2 October 2020 / Accepted: 15 December 2020 / Published online: 3 January 2021
© The Author(s), under exclusive licence to Springer-Verlag GmbH, DE part of Springer Nature 2021

Abstract

In this research, the various physical properties of Nb-doped SrFeO₃ were investigated using the density functional theory (DFT), which was not experimentally investigated and reported in the previous literature. This is the first detailed theoretical study about these properties of this doped system. The calculated lattice parameters exhibited excellent conformity with the experimental data. In addition, the structural and mechanical stability of the studied compound was confirmed by the negative value of formation enthalpy and elastic constants (fulfilled the Born stability criteria), respectively. The metallic nature of SrFe_{0.5}Nb_{0.5}O₃ was revealed by their band structure and the density of states. A strong hybridization was observed among Fe-3*d*, Nb-4*p*, and O-2*p* states at the Fermi level, reflecting the covalent bonding of Fe/Nb–O. Furthermore, the mechanical properties including the elastic moduli, Poisson ratio, Pugh's ratio, hardness, and machinability index of SrFe_{1-x}Nb_xO₃ (*x* = 0.4, 0.5, and 0.6), were also studied in depth, and showed considerable effects of doping. Finally, a high level of anisotropy was noticed for SrFe_{0.5}Nb_{0.5}O₃. Therefore, our simulation output clearly illustrated the influence of Nb doping in the theoretical results of the physical properties of the presently studied strontium ferrite.

Keywords Perovskite material · Structural properties · Electronic properties · Mechanical properties · Anisotropy

1 Introduction

The general formula of perovskite materials is ABO₃, and they are usually crystallized with cubic symmetry in the space group of *Pm-3m* [1, 2]. These compounds have the simplest crystal structure and many interesting properties,

such as ferroelectricity, magnetoresistance, superconductivity, piezoelectricity, and ionic conductivity, all of which make them attractive research subjects [3–5]. This type of materials is mostly suited for the construction of optoelectronic modulators, infrared sensors and detectors, memory storage devices, and microwave device capacitors [6–9]. Currently, perovskite materials are also used in solid oxide fuel cells to produce electrodes [10, 11]. Strontium ferrite (SrFeO₃) is one of the most influential perovskites, which has a mixed oxygen-ion and electron conductivity at a temperature range of 600–900 °C, as well as stability in reducing conditions [12, 13]. Therefore, SrFeO₃ should be suitable for solid oxide fuel cells, oxygen sensors, and oxygen permeation membranes [14–16]. Complex iron-based perovskite-type materials with the chemical formula A(Fe_{0.5}B_{0.5})O₃ have recently been gained great attention, where A = Ca, Ba, Sr; and B = Nb, Ta, Sb [17–22]. This attraction occurs because these materials exhibit high-dielectric permittivity across a broad range of temperature. Moreover, these materials are essential in microelectronics and have diverse technological uses, including memory modules and actuators, sensors, multilayer capacitors,

✉ Khandaker Monower Hossain
monower37@gmail.com

¹ Department of Electrical and Electronic Engineering, International Islamic University Chittagong, Kumira, Chittagong 4318, Bangladesh

² Department of Materials Science and Engineering, University of Rajshahi, Rajshahi 6205, Bangladesh

³ Bangamata Sheikh Fojilatunnesa Mujib Science and Technology University, Jamalpur 2012, Bangladesh

⁴ Department of Electronic and Telecommunication Engineering, Bangabandhu Sheikh Mujibur Rahman Science and Technology University, Gopalganj 8100, Bangladesh

⁵ Department of Arts and Sciences, Bangladesh Army University of Science and Technology, Nilphamari, Saidpur 5310, Bangladesh

detectors, and microwave frequency resonators [17–22]. For the complex perovskites, $A(B'B'')O_3$, their characteristics are dependent on the B sublattice cation scheme and are regulated mainly by the charge difference between the B site cations and partly by the ionic size difference between B' and B'' [17]. Saha and Sinha [20] investigated the crystal structural of $SrFe_{0.5}Nb_{0.5}O_3$ in the monoclinic phase. In addition, $SrFe_{0.5}Nb_{0.5}O_3$ was also successfully refined with the cubic and orthorhombic phases [23, 24]. Moreover, both $SrFeO_3$ and $SrFe_{0.5}Nb_{0.5}O_3$ ceramics were further synthesized via a high-temperature solid-state reaction technique [17], and the pure $SrFeO_3$ was refined with a cubic structure of $Pm\bar{3}m$ space group consistent with previously published findings [25–27]. However, the structure shifted to tetragonal symmetry with a $P4mm$ space group when 50 percent Nb^{5+} was doped at Fe^{4+} sites [17]. The permittivity and loss function of $SrFe_{0.5}Nb_{0.5}O_3$ were examined using a frequency range of 50 Hz–2 MHz and a temperature range of 143–473 K [20]. Since, doping has a profound effect on a material's property, further investigation is necessary on Nb-doped $SrFeO_3$ perovskite. Although the aforementioned experimental studies have provided interesting findings, there is much left to explore. To understand a material system properly, it is important to explore its physical aspects, such as electronic, mechanical, anisotropic properties, and so on, as these properties can reflect a clear prediction about the material's feasible applications. But the previous experimental investigations on Nb-doped $SrFeO_3$ did not unfold these necessary attributes. Although a few theoretical investigations on undoped $SrFeO_3$ were performed [25–27], no such study on $SrFe_{1-x}Nb_xO_3$ is available in the existing literature. So, the discovery of physical properties of $SrFe_{1-x}Nb_xO_3$ has become an enthusiastic topic for the researchers that motivated us for further investigation on it to more precisely understand this perovskite system. Recently, the first-principle calculation based on the density functional theory (DFT) method has become the most reliable theoretical approach for the investigation of physical properties of solid materials. In addition, this method is relatively simple and easier to investigate the material's properties as compared to the different experimental methodology. In recent years, a considerable number of research works on the perovskite materials have been performed by DFT method and published in the highly reputed scientific journals by many researchers [28–31]. Therefore, we employed the DFT-based Cambridge Serial Total Energy Package (CASTEP) to calculate and explore the structural, electronic, mechanical, and anisotropic properties of $SrFe_{1-x}Nb_xO_3$ ($x=0.4, 0.5$, and 0.6) to grasp the detailed knowledge about this system so that the scientific community can exploit this material

system to the practical uses according to the suitability of different properties.

2 Computational details

The compound $SrFe_{0.5}Nb_{0.5}O_3$ was crystallized in a tetragonal structure with the space group of $P4mm$ (No. 99) [17]. At first, the equilibrium crystal structure was drawn by considering the experimentally reported lattice constants, $a=3.9656$, and $c=3.9795$, and the Wyckoff positions $1a$ (0, 0, 0) for Sr; $1b$ (0.5, 0.5, 0.5041) for randomly distributed Nb and Fe; $1b$ (0.5, 0.5, 0.0340) for O1; and $2c$ (0.5, 0, 0.4569) for O2 [17]. Though the compounds $SrFe_{0.6}Nb_{0.4}O_3$ and $SrFe_{0.4}Nb_{0.6}O_3$ are not experimentally synthesized, we can simulate it using the crystallographic data of $SrFe_{0.5}Nb_{0.5}O_3$. The first-principle calculations were implemented to explore the structural, electronic, and mechanical properties of the titled perovskite using CASTEP code [32] in the context of DFT [33], based on the pseudo-potential plane-wave (PP-PW) total energy calculation. The Vanderbilt-type ultrasoft pseudopotential [34] was chosen for the interaction between electrons and ion nuclei. Next, the exchange correlation energy was formalized through the Generalized Gradient Approximation (GGA) composed of the Perdew-Burke-Ernzerhof (PBE) [35]. A cut-off energy of 900 eV was selected to ensure the convergence. The Monkhorst–Pack scheme [36] was used with the k -points of $12 \times 12 \times 12$ sampling integration, which were fixed to ultrafine quality over the first Brillouin zone to optimize the crystal structure. Using the Broyden–Fletcher–Goldfarb–Shanno (BFGS) algorithm [37], the lattice constants and internal atomic coordinates were assessed. All of the lattice parameters and atomic positions were relaxed during the process of structural optimization [38, 39]. In addition, the unit cell and atomic relaxation were conducted considering the maximum ionic displacement of 5.0×10^{-4} Å, the total energy of 5.0×10^{-6} eV/atom, the maximum stress of 0.02 GPa, and the maximum ionic force of 0.01 eV/Å. Moreover, the virtual crystal approximation (VCA) method was used to add Nb at Fe-site, therefore, Fe and Nb are randomly distributed at $1b$ (0.5, 0.5, 0.5041) Wyckoff position. In the VCA, the crystal preserves the primitive periodicity with mixture of atoms. Using this method, the relative concentrations can be set for any number of atoms involved, where the total concentration of the substituted and substituent atoms is always 100%. VCA is an alternative to the construction of super cell approach, which is suitable for calculating the properties of doped systems. Recently, a considerable number of research articles have been published in the reputed journals based on the calculations of VCA method [40–43]. The electronic and mechanical properties were calculated by considering the

mentioned parameters. Moreover, the “stress–strain” method [44] was used to calculate the elastic constants and the elastic moduli.

3 Results and discussions

3.1 Structure and phase stability

Formation enthalpy (ΔH_f) is one of the most crucial factors in predicting the crystal stability of a solid [45, 46]. In this study, we did not use any temperature or pressure to calculate energy. Therefore, the formation enthalpy was equal to the formation energy i.e., $\Delta E_f = \Delta H_f$, which can be expressed as follows:

$$\Delta H_f = \Delta E_f(\text{SrFe}_{1-x}\text{Nb}_x\text{O}_3) = [E_{\text{tot}}(\text{SrFe}_{1-x}\text{Nb}_x\text{O}_3) - E_s(\text{Sr}) - (1-x)E_s(\text{Fe}) - xE_s(\text{Nb}) - 3E_s(\text{O})]/N, \quad (1)$$

here, $E_s(\text{Sr})$, $E_s(\text{Fe})$, $E_s(\text{Nb})$, and $E_s(\text{O})$ are the energies of the Sr, Fe, Nb, and O atoms, respectively; as well as $E_{\text{tot}}(\text{SrFe}_{1-x}\text{Nb}_x\text{O}_3)$ describes the total energy of $\text{SrFe}_{1-x}\text{Nb}_x\text{O}_3$ ($x=0.4, 0.5$, and 0.6) and N is the total number of atoms. The negative values of formation enthalpy (Table 1) ensured the chemical and thermodynamical stability of Nb-doped SrFeO_3 . The conventional optimized crystal structure of $\text{SrFe}_{1-x}\text{Nb}_x\text{O}_3$ is presented in Fig. 1. The calculated lattice constants and unit cell volume are listed in Table 1, and these were very close to the existing experimental data [17], ensuring the accuracy of our calculations. Moreover, our simulated data are also compared with the previous experimental and theoretical results of pure cubic SrFeO_3 and SrNbO_3 [17, 27, 47–50] in Table 1. To our knowledge, no theoretical study is yet available on Nb-doped SrFeO_3 , and

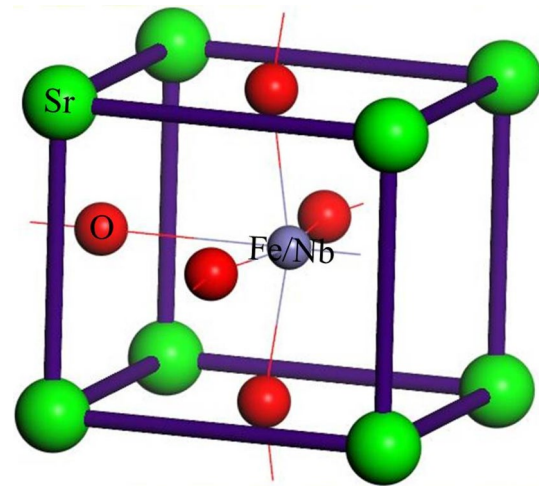


Fig. 1 The conventional optimized crystal structure of $\text{SrFe}_{1-x}\text{Nb}_x\text{O}_3$ ($x=0.4, 0.5$, and 0.6)

therefore, we cannot compare our results with the calculations of other research groups.

3.2 Electronic properties

Band structure (BS), density of states (DOS), and charge density mapping are the fundamental parameters for understanding the electronic behavior of a material [51–54]. To clarify the electronic properties in this study, we also investigated the BS and DOS of $\text{SrFe}_{0.5}\text{Nb}_{0.5}\text{O}_3$, as respectively represented in Figs. 2 and 3. The Fermi level (E_F) was set to 0 eV and coincided with the top of the valence band. As shown in Fig. 2, several bands have crossed the E_F , and no band gap was observed; hence, the compound displayed

Table 1 The lattice constant, a (Å), volume, V (Å³), and formation enthalpy, ΔH_f (eV/atom) of tetragonal $\text{SrFe}_{1-x}\text{Nb}_x\text{O}_3$ ($x=0.4, 0.5$, and 0.6) compared with the experimental and simulation results of cubic SrFeO_3 and SrNbO_3

Compound	a	c	V	ΔH_f	Remarks
$\text{SrFe}_{0.6}\text{Nb}_{0.4}\text{O}_3$	3.6153	4.1131	53.7613	−17.58	This work
$\text{SrFe}_{0.5}\text{Nb}_{0.5}\text{O}_3$	3.6163	4.0057	52.3888	−22.13	This work
	3.9656	3.9795	–	–	[17] ^{Expt}
$\text{SrFe}_{0.4}\text{Nb}_{0.6}\text{O}_3$	3.5625	4.0803	51.7852	−25.97	This work
SrFeO_3	3.922	–	60.343	–	[27] ^{Theo}
	3.834	–	56.379	−6.54	[47] ^{Theo}
	3.870	–	–	–	[17] ^{Expt}
SrNbO_3	4.052	–	–	–	[48] ^{Theo}
	4.073	–	–	–	[49] ^{Theo}
	4.024	–	–	–	[50] ^{Expt}

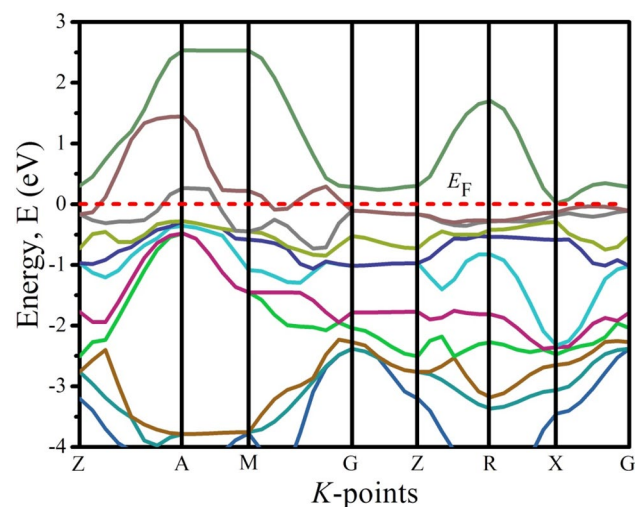


Fig. 2 Band structure of $\text{SrFe}_{0.5}\text{Nb}_{0.5}\text{O}_3$. The red horizontal dashed line located at 0 eV is the Fermi level, E_F

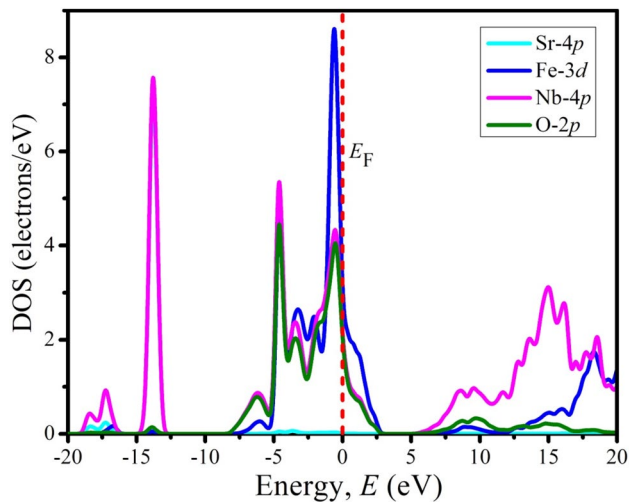


Fig. 3 Density of states of $\text{SrFe}_{0.5}\text{Nb}_{0.5}\text{O}_3$. The red vertical dashed line located at 0 eV is the Fermi level, E_F

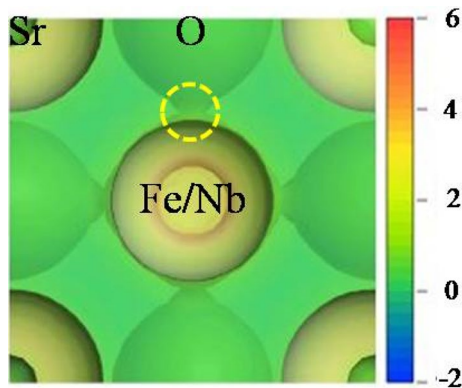


Fig. 4 The 2D charge density difference mapping of $\text{SrFe}_{0.5}\text{Nb}_{0.5}\text{O}_3$

metallic behavior. The metallic nature was also observed for pure SrFeO_3 and SrNbO_3 in the previous literature [27, 47, 48]. Notably, a conduction band near the E_F is flat along the G to Z direction which may have enhanced the pairing of electrons responsible for the compound's superconducting nature [45].

In the case of the DOS profile (Fig. 3), a strong hybridization was observed at the E_F among Fe-3d, Nb-4p, and

O-2p states. The individual contribution of Fe-3d was higher than the other contributions. However, the valance bands below the E_F originated mainly due to the contributions of Nb-4p and O-2p, with a minor contribution of the Fe-3d state. There were two peaks in the valance band region, predominantly manifested by the 4p and 2p orbitals of the Nb and O atoms. On the other hand, the conduction bands above the E_F resulted from the major contributions of the Nb-4p and the minor contributions of the Fe-3d and O-2p orbitals. Interestingly, the values of DOS in the vicinity of E_F made the compound conductive.

We investigated the charge density difference mapping with the help of a charge density scale interns of light intensity. In the scale, higher electron density is indicated in red, and lower electron density is represented by blue. It is clear from the Fig. 4 that electron density was relatively higher for Fe/Nb than for Sr and O. At the same time, there was no overlapping between the Sr and O atoms. On the other hand, a clear overlapping existed between the Fe/Nb and O. Therefore, a covalent bonding existed in Fe/Nb–O along with the transfer of charge between the Fe/Nb and O atoms.

3.3 Elastic constants and mechanical properties

Elastic constant is one of the fundamental tools used to identify the mechanical stability, hardness, stiffness, ductile–brittle behavior, and machinability index of a solid [55, 56]. The tetragonal crystal system $\text{SrFe}_{1-x}\text{Nb}_x\text{O}_3$ ($x=0.4, 0.5, \text{ and } 0.6$) has six distinct elastic constants (C_{11} , C_{12} , C_{13} , C_{33} , C_{44} , and C_{66}), which are listed in Table 2. To become stable system, the elastic constants of a tetragonal material must fulfill the following Born stability conditions [57].

$$\begin{aligned} C_{11} > 0, C_{33} > 0, C_{44} > 0, C_{66} > 0 \\ C_{11} - C_{12} > 0, C_{11} + C_{33} - 2C_{13} > 0 \\ 2(C_{11} + C_{12}) + C_{33} + 4C_{13} > 0. \end{aligned} \quad (2)$$

The elastic constants of $\text{SrFe}_{1-x}\text{Nb}_x\text{O}_3$ completely justified the aforementioned conditions, ensuring the mechanical stability of this system. Since the values of C_{11} were greater than that of C_{33} for all the doped systems, the bonding energy was considerably higher in the [010] and [100] directions than in the [001] direction. Therefore, the

Table 2 The calculated elastic constants, C_{ij} (GPa) of tetragonal $\text{SrFe}_{1-x}\text{Nb}_x\text{O}_3$ ($x=0.4, 0.5, \text{ and } 0.6$) compared with cubic SrFeO_3 and SrNbO_3

Compound	C_{11}	C_{12}	C_{13}	C_{33}	C_{44}	C_{66}	Remarks
$\text{SrFe}_{0.6}\text{Nb}_{0.4}\text{O}_3$	259.14	157.40	102.53	113.12	58.01	110.69	This work
$\text{SrFe}_{0.5}\text{Nb}_{0.5}\text{O}_3$	241.25	170.56	95.5	112.39	66.54	113.21	This work
$\text{SrFe}_{0.4}\text{Nb}_{0.6}\text{O}_3$	231.87	199.05	105.75	93.53	69.47	128.25	This work
SrFeO_3	144.87	150.18	–	–	108.39	–	[27] ^{Theo}
	158	155	–	–	108	–	[47] ^{Theo}
SrNbO_3	364.05	102.65	–	–	57.98	–	[48] ^{Theo}

compressibility along [001] was weaker than in the [100] direction [58]. Moreover, C_{44} is smaller than C_{66} ; thus, shear deformation occurred more readily along the [001] direction than along the [010] direction. However, $C_{11} + C_{12} > C_{33}$, hence, the bonding in the (001) plane and the elastic tensile modulus on that plane were elastically more rigid and higher along the c -axis. It can be seen that all the elastic constants varied with increasing doping content of Nb^{5+} (Table 2), therefore, it is not difficult to understand the effects of doing in this system.

The bulk modulus (B) and shear modulus (G) were determined using the well-known Voigt–Reuss–Hill approximations [59–61].

$$B_V = \frac{2}{9} \left(C_{11} + C_{12} + 2C_{13} + \frac{C_{12}}{2} \right), \quad (3)$$

$$B_R = \frac{C^2}{M}, \quad (4)$$

where $C^2 = (C_{11} + C_{12})C_{33} - 2C_{13}^2$ and $M = (C_{11} + C_{12} + 2C_{33} - 4C_{13})$

$$G_V = \frac{(M + 3C_{11} - 3C_{12} + 12C_{44} + 6C_{66})}{30}, \quad (5)$$

$$G_R = \frac{15}{\left(\frac{18B_V}{C^2} + \frac{6}{(C_{11}-C_{12})} + \frac{6}{C_{44}} + \frac{3}{3C_{44}} \right)}, \quad (6)$$

$$B = \frac{1}{2}(B_V + B_R); \quad G = \frac{1}{2}(G_V + G_R), \quad (7)$$

$$Y = \frac{9BG}{3B + G}; \quad \nu = \frac{3B - 2G}{2(3B + G)}. \quad (8)$$

To determine Young's modulus Y and Poisson's ratio ν , we employed the above Eqs. (8). Table 3 provides our estimated B , G , Y , and ν for $\text{SrFe}_{1-x}\text{Nb}_x\text{O}_3$ ($x=0.4, 0.5$, and 0.6).

The bulk modulus can evaluate the bonding strength among the constituent atoms within a solid [62]. Strong bonding was observed in $(\text{Zr}_{1-x}\text{Ti}_x)_2\text{AlC}$, which had a bulk modulus of 128 GPa [63]. Therefore, the bulk modulus of 131.43, 128.30, and 122.57 GPa may reflect the strong bonding of atoms in $\text{SrFe}_{1-x}\text{Nb}_x\text{O}_3$ for $x=0.4, 0.5$, and 0.6 , respectively, and with increasing doping, the bonding strength may slightly decrease. Notably, the bulk and shear modulus reflect the resistance of a solid against volume and shape change, respectively [64, 65]. The higher B with lower G demonstrated the damage tolerance, machinability, and stiffness of $\text{SrFe}_{1-x}\text{Nb}_x\text{O}_3$. All the elastic moduli B , G , and Y were relatively large; therefore, this study predicted the greater hardness of $\text{SrFe}_{1-x}\text{Nb}_x\text{O}_3$.

Beyond this, Pugh's ratio (B/G), Poisson's ratio (ν), and Cauchy pressure ($C_{12}-C_{44}$) are three important parameters for the identification of a material's ductile or brittle nature. If $C_{12}-C_{44}$ is negative, a material is brittle; otherwise, it is ductile. If a material has $B/G > 1.75$, it will show ductile behavior; on the other hand, if $B/G < 1.75$, the material will be brittle. Moreover, Frantsevich emphasized the critical value of ν as 0.26, above which a material is ductile [66]. Judging from the values of the aforementioned three indicators (Table 3), we concluded that the studied compounds are ductile in nature. In addition, Vicker's hardness (H_V) was calculated using the following expression [67] and the calculated values are mentioned in Table 3.

$$H_V = \frac{(1 - 2\nu)Y}{6(1 + \nu)}. \quad (9)$$

It is well established that diamond is the hardest material on earth. It has a Vicker's hardness value in the range of 70–150 GPa. The calculated values of H_V are 8.13, 7.72, and 5.83 GPa, respectively, for $\text{SrFe}_{0.6}\text{Nb}_{0.4}\text{O}_3$, $\text{SrFe}_{0.5}\text{Nb}_{0.5}\text{O}_3$, and $\text{SrFe}_{0.4}\text{Nb}_{0.6}\text{O}_3$, which means that $\text{SrFe}_{1-x}\text{Nb}_x\text{O}_3$ is an extremely soft material compared with diamond. In addition, the hardness of this compound was reduced with increasing doping of Nb, as the bonding strength slightly decreased with increasing doping predicted by their bulk modulus.

Table 3 Cauchy pressure, $C_{12}-C_{44}$, bulk modulus, B (GPa), shear modulus, G (GPa), Young's modulus, Y (GPa), Pugh's ratio (B/G), machinability index, μ_M , Poisson's ratio, ν , and Vickers hardness, H_V

(GPa) of tetragonal $\text{SrFe}_{1-x}\text{Nb}_x\text{O}_3$ ($x=0.4, 0.5$, and 0.6) compared with cubic SrFeO_3 and SrNbO_3

Compound	$C_{12}-C_{44}$	B	G	Y	B/G	μ_M	ν	H_V	Remarks
$\text{SrFe}_{0.6}\text{Nb}_{0.4}\text{O}_3$	99.39	131.43	57.19	149.84	2.29	2.26	0.29	8.13	This work
$\text{SrFe}_{0.5}\text{Nb}_{0.5}\text{O}_3$	104.02	128.30	57.78	150.72	2.22	1.92	0.30	7.72	This work
$\text{SrFe}_{0.4}\text{Nb}_{0.6}\text{O}_3$	129.58	122.57	48.41	128.35	2.53	1.76	0.32	5.83	This work
SrFeO_3	–	148.41	28.54	80.47	5.20	1.36	0.40	1.91	[27] ^{Theo}
	47	158	38	99	4.15	1.46	0.34	3.94	[47] ^{Theo}
SrNbO_3	–	189.78	80.82	212.33	2.35	–	0.31	–	[48] ^{Theo}

Although this Nb-doped perovskite material is far softer than diamond, however, it is hard enough for conventional applications. On a related note, the machinability index (μM) is becoming more important in industrial applications. This value can determine the cutting force of a material, plastic strain, and optimum economic level of machine utilization. This index is associated with the machinability of a material according to the following expression [68]:

$$\mu\text{M} = \frac{B}{C_{44}}. \quad (10)$$

The computed values of μM are listed in Table 3, and the μM for $\text{SrFe}_{0.6}\text{Nb}_{0.4}\text{O}_3$ and $\text{SrFe}_{0.5}\text{Nb}_{0.5}\text{O}_3$ were higher than the values of certain other compounds [69, 70], implying a relatively high level of machinability, but became smaller for $\text{SrFe}_{0.4}\text{Nb}_{0.6}\text{O}_3$.

To demonstrate more clear picture, the elastic constants and mechanical data of cubic perovskites SrFeO_3 and SrNbO_3 were also presented in Table 2 and Table 3, showing discrepancy in most of the cases from the tetragonal $\text{SrFe}_{1-x}\text{Nb}_x\text{O}_3$ ($x=0.4, 0.5,$ and 0.6), because of different crystal system and varying compositions.

3.4 Elastic anisotropy

Elastic anisotropy is another absorbing physical parameter of solid materials relevant to elastic properties. A solid's mechanical durability, microscopic behavior of solid materials, applications under diverse external stress of a solid, and degree of elastic anisotropy are all crucial for both single and polycrystalline solids. They can be considerably developed by analyzing a substance's degree of elastic anisotropy [45]. Therefore, a proper illustration of various elastic anisotropic behaviors can play an essential role in the basic solid-state science as well as in applied engineering sciences for improving devices, where mechanical properties and stress can influence performance and reliability [69–71]. In addition, the shear anisotropic factors of a crystal can be manifested via the following expressions [72]:

For $\{100\}$ or $\{010\}$ shear plane,

$$A_1 = \frac{C_{44}(C_{11} + 2C_{13} + C_{33})}{(C_{11}C_{33} - C_{13}^2)}. \quad (11)$$

For the $\{1\bar{1}0\}$ shear plane,

$$A_2 = \frac{C_{44}(C_L + 2C_{13} + C_{33})}{(C_L C_{33} - C_{13}^2)}. \quad (12)$$

For the $\{001\}$ shear planes,

Table 4 Calculated Shear anisotropic factors A_i ($i=1-3$), anisotropy in bulk modulus (A_B), anisotropy in shear modulus (A_G), and universal anisotropy index (A^U) of tetragonal $\text{SrFe}_{0.5}\text{Nb}_{0.5}\text{O}_3$ compound

A_1	A_2	A_3	A_B (%)	A_G (%)	A^U
2.014	1.847	3.203	0.141	0.122	1.715

$$A_3 = \frac{2C_{66}}{(C_{11} - C_{12})}, \quad (13)$$

where, $C_L = \frac{C_{66} + (C_{11} + C_{12})}{2}$. Table 4 incorporated the calculated anisotropic factors. The values of A_1 , A_2 , and A_3 are equal to unity ($=1$) for an isotropic crystal, whereas any value higher or lower than unity is a measure of the degree of shear anisotropy endowed by the crystal [71, 73]. Table 4 clearly shows that A_1 , A_2 , and A_3 indicate the highly anisotropic nature of our studied material. The elastic anisotropy percentage in bulk (A_B) and in the shear modulus (A_G) were evaluated using the following common expressions [73]:

$$A_B = \frac{B_V - B_R}{B_V + B_R}, \quad (14)$$

$$A_G = \frac{G_V - G_R}{G_V + G_R}, \quad (15)$$

here, V and R , respectively, describe the Voigt and Reuss approximations. The zero value represents a perfect isotropic nature, whereas the deviation from zero indicates an anisotropic nature, up to 100%, which indicates the highest anisotropy. The calculated A_B and A_G values in Table 4, indicate the high anisotropic nature in a similar manner of shear anisotropic factors.

The universal anisotropy index A^U is an important indicator that permitted us to calculate the anisotropy and can be expressed as [73]:

$$A^U = 5\frac{G_V}{G_R} + \frac{B_V}{B_R} - 6. \quad (16)$$

The value of A^U is zero for isotropic solid materials. The calculated value of A^U determines the degree of elastic anisotropy, which was also verified by the use of various anisotropy indices in our previous discussion.

To visually interpret the anisotropy, it was described by 3D surface constructions (3D contour plots) and their planar projections (2D contour plots) of elastic moduli. The 2D and 3D anisotropy contour plots of Young's modulus, Y (GPa), shear modulus, G (GPa), and Poisson's ratio, ν of $\text{SrFe}_{0.5}\text{Nb}_{0.5}\text{O}_3$ obtained using the ELATE program [74] are shown in Fig. 5. These plots were generated from the calculated values of C_{ij} of $\text{SrFe}_{0.5}\text{Nb}_{0.5}\text{O}_3$. For an isotropic crystal, the 3D surface construction graph should

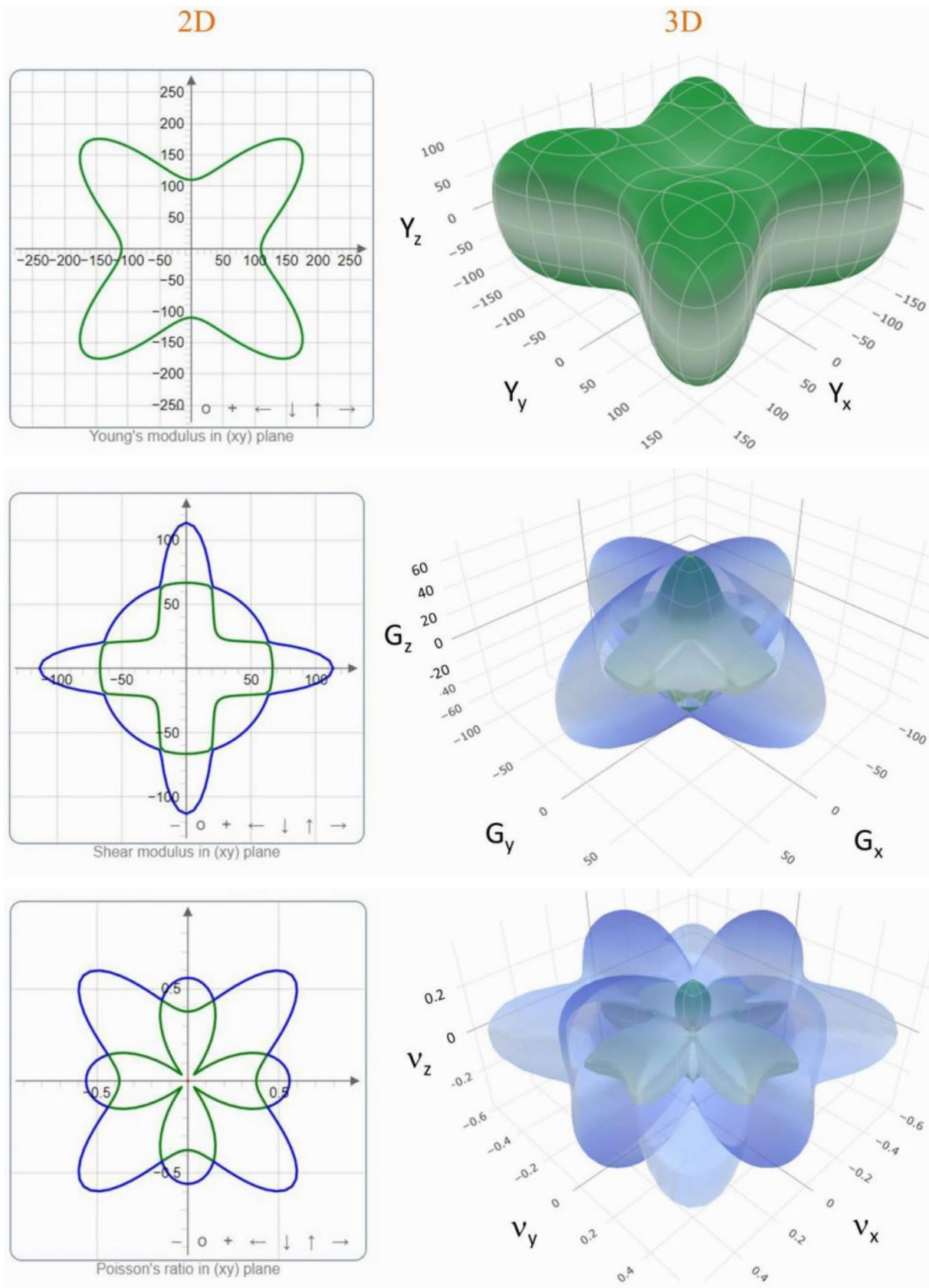


Fig. 5 Anisotropy of Young's modulus, Y (GPa), shear modulus, G (GPa) and Poisson's ratio, ν in 2D (left panel) and 3D (right panel) contour plots of $\text{SrFe}_{0.5}\text{Nb}_{0.5}\text{O}_3$

Table 5 The minimum and maximum limits of Young's modulus (Y), Shear modulus (G), and Poisson's ratio (ν) for tetragonal $\text{SrFe}_{0.5}\text{Nb}_{0.5}\text{O}_3$ compound

Young's Modulus/GPa		Shear Modulus/GPa		Poisson's ratio	
Y_{\min}	Y_{\max}	G_{\min}	G_{\max}	ν_{\min}	ν_{\max}
110.09	187.46	32.71	113.21	0.120	0.508

Table 6 The calculated values of Young's Modulus (Y), Shear Modulus (G), and Poisson's ratio (ν) in three principal directions for tetragonal $\text{SrFe}_{0.5}\text{Nb}_{0.5}\text{O}_3$ compound

Y (in GPa)			G (in GPa)			ν		
Y_x	Y_y	Y_z	G_x	G_y	G_z	ν	ν_y	ν_z
135.72	136.33	181.12	47.61	48.53	89.87	0.287	0.290	0.398

be spherical; otherwise, the crystal reflects an anisotropic nature. The deviation of the spherical 3D surface measures the degree of elastic anisotropy level of solids. Clearly, our studied material displayed a highly anisotropic nature, which was consistent with the previous calculations of anisotropy indices. Table 5 shows the minimum and maximum values of these three parameters for the $\text{SrFe}_{0.5}\text{Nb}_{0.5}\text{O}_3$ compound at different directions to contrast the anisotropic nature of the elastic moduli.

In addition, the values of Shear Modulus, Poisson's ratio, and Young's Modulus, in three principal crystallographic directions are listed in Table 6. The anisotropy of elastic moduli occurred in a sequence of $Y < G < \nu$, according to 3D surface constructions and their 2D planar projections presentations.

4 Conclusions

In brief, the structural, electronic, mechanical, and anisotropic properties of Nb-doped SrFeO_3 perovskite were comprehensively investigated in this study. The structural and mechanical stability of $\text{SrFe}_{1-x}\text{Nb}_x\text{O}_3$ ($x = 0.4, 0.5$, and 0.6) was, respectively, proved by the calculated formation enthalpy and elastic constants. The band diagram exhibited the metallicity of $\text{SrFe}_{0.5}\text{Nb}_{0.5}\text{O}_3$, which was confirmed by the strong hybridization among Fe-3d, Nb-4p, and O-2p states at the Fermi level. In addition, charge density mapping demonstrated the covalent bonding of Fe/Nb-O in $\text{SrFe}_{0.5}\text{Nb}_{0.5}\text{O}_3$. The variation of elastic constant and elastic moduli with the variation of Nb addition at Fe-site reflected the doping effects in this system. Furthermore, the mechanical properties of $\text{SrFe}_{1-x}\text{Nb}_x\text{O}_3$ ($x = 0.4, 0.5$, and 0.6) revealed the ductile nature and relatively high hardness of this perovskite, which in turn reduced the hardness and machinability with the increment of Nb doping. Finally,

$\text{SrFe}_{0.5}\text{Nb}_{0.5}\text{O}_3$ displayed a high degree of anisotropy. Such a study would be helpful to the scientific community to choose their application area according to their desired properties.

Author contributions MZH investigation, methodology, data curation, and writing original draft. KMH formal analysis, conceptualization, supervision, and review-editing. SKM formal analysis, writing original draft, and review-editing. MR formal analysis, validation, and review-editing. JKM formal analysis, and review-editing. MAR formal analysis and review-editing.

Data availability All data needed to evaluate the conclusion of this study are presented in the paper. Additional data are available from the corresponding author upon reasonable request.

Compliance with ethical standards

Conflict of interest The authors declare no conflict of interests.

References

1. T. Wolfram, S.E. Llialtiog-Lu, *Electronic and Optical Properties of D-Band Perovskites* (Cambridge University Press, Cambridge, 2006).
2. Z. Feng, H. Hu, S. Cui, C. Bai, *Solid State Commun.* **148**, 472 (2008)
3. G. Murtaza, I. Ahmad, B. Amin, A. Afaq, M. Maqbool, J. Maqsood, I. Khan, M. Zahid, *Opt. Mat.* **33**, 553 (2011)
4. S.K. Sack, I. Hofelich, *Z. Naturforsch. B* **26**, 539 (1971)
5. Z. Ali, I. Ahmad, I. Khan, B. Amin, *Intermetallics* **31**, 287 (2012)
6. J.F. Scott, *Science* **315**, 954 (2007)
7. E. Cross, *Nature* **432**, 24 (2004)
8. T. Schneider, D. Leduc, J. Cardin, C. Lupi, N. Barreau, H. Gundel, *Opt. Mater.* **29**, 1871 (2007)
9. R. Watton, *Ferroelectrics* **91**, 87 (1989)
10. B.C.H. Steele, A. Heinzl, *Nature* **414**, 345 (2001)
11. A.J. Jacobson, *Chem. Mater.* **22**, 660 (2010)
12. A. Holt, T. Norby, R. Glenne, *Ionics* **5**, 434 (1999)

13. M.V. Patrakeev, I.A. Leonidov, V.L. Kozhevnikov, V.V. Kharton, *Solid State Sci.* **6**, 907 (2004)
14. J. Yoo, A. Verma, S. Wang, A.J. Jacobson, *J. Electrochem. Soc.* **152**, A497 (2005)
15. V. Zaspalis, A. Evdou, L. Nalbandian, *Fuel* **89**, 1265 (2010)
16. Y. Niu, W. Zhou, J. Sunarso, L. Ge, Z. Zhu, Z. Shao, *J. Mater. Chem.* **20**, 9619 (2010)
17. M.J. Akhtar, R.T.A. Khan, *Mater. Charact.* **62**, 1016 (2011)
18. Z. Wang, Chen XM. *J. Phys. D Appl Phys* **42**, 175005 (2009)
19. I.P. Raevski, S.A. Prosandeev, A.S. Bogatin, M.A. Malitskaya, L. Jastrabik, *J. Appl. Phys.* **93**, 4130 (2003)
20. S. Saha, T.P. Sinha, *J. Appl. Phys.* **99**, 014109 (2006)
21. S. Saha, T.P. Sinha, *J. Phys. Cond. Matter.* **14**, 249 (2002)
22. U. Intatha, S. Eitssayeam, J. Wang, T. Tunkasiri, *Curr. Appl. Phys.* **10**, 21 (2010)
23. N. Rama, J.B. Philipp, M. Opel, *J. Appl. Phys.* **95**, 7528 (2004)
24. R. Rodriguez, A. Fernandez, A. Isalgue, J. Rodriguez, A. Labarta, J. Tejada, *J. Phys. C: Solid State Phys.* **18**, L401 (1985)
25. N. Hamdad, H. Rozale, A. Lakdja, A. Chahed, O. Benhelal, *Superlattices Microstruct.* **63**, 182 (2013)
26. I.R. Shein, K.I. Shein, V.L. Kozhevnikov, A.L. Ivanovskii, *Phys. Solid State* **47**, 2082 (2005)
27. M.Z. Hasan, M. Rasheduzzaman, K.M. Hossain, *Chin. Phys. B* (2020). <https://doi.org/10.1088/1674-1056/abab7f>
28. L. Feng, Z. Liu, Q. Liu, *Phys. B* **407**, 2009 (2012)
29. L.P. Ding, P. Shao, F.H. Zhang, C. Lu, L. Ding, S.Y. Ning, X.F. Huang, *Inorg. Chem.* **255**, 7033 (2016)
30. M.Z. Rahaman, A.K.M.A. Hossain, *RSC Adv.* **8**, 33010 (2018)
31. M.N. Islam, M.A. Hadi, J. Podder, *AIP Adv.* **9**, 125321 (2019)
32. M.D. Segall, P.J.D. Lindan, M.J. Probert, C.J. Pickard, P.J. Hasnip, S.J. Clark, M.C. Payne, *J. Phys.: Cond. Matter* **14**, 2717 (2002)
33. M.C. Payne, M.P. Teter, D.C. Allan, T.A. Arias, J.D. Joannopoulos, *Rev. Mod. Phys.* **64**, 1045 (1992)
34. D. Vanderbilt, *Phys. Rev. B* **41**, 7892 (1990)
35. J.P. Perdew, K. Burke, M. Ernzerhof, *Phys. Rev. Lett.* **77**, 3865 (1996)
36. H.J. Monkhorst, J.D. Pack, *Phys. Rev.* **13**, 5188 (1976)
37. T.H. Fischer, J. Almlof, *J. Phys. Chem.* **96**, 9768 (1992)
38. Z. Boekelheide, T. Saerbeck, A.P.J. Stampfl, R.A. Robison, D.A. Stewart, F. Hellman, *Phys. Rev. B* **85**, 094413 (2012)
39. Y. Pan, M. Wen, *Int. J. Hydrogen Energy* **43**, 22055 (2018)
40. E.Z. Solvas, M.A. Hadi, D. Horlait, D.C. Parfitt, A. Thibaud, A. Chroneos, W.E. Lee, *J. Am. Ceram. Soc.* **100**, 3393 (2017)
41. A.R. Degheidy, S.A.A. Elwakil, E.B. Elkenany, *J. Alloys Compd.* **574**, 580 (2013)
42. M.A. Hadi, M. Roknuzzaman, A. Chroneos, S.H. Naqib, A.K.M.A. Islam, R.V. Vovk, K. Ostrikov, *Comput. Mater. Sci.* **137**, 318 (2017)
43. D. Yang, L.L. Wei, X.L. Chao, Z.P. Yang, X.Y. Zhou, *Phys. Chem. Chem. Phys.* **18**, 7702 (2016)
44. C.Z. Fan, S.Y. Zeng, L.X. Li, Z.J. Zhan, R.P. Liu, W.K. Wang, P. Zhang, Y.G. Yao, *Phys. Rev. B* **74**, 125118 (2006)
45. M.H.K. Rubel, K.M. Hossain, S.K. Mitro, M.M. Rahaman, M.A. Hadi, A.K.M.A. Islam, *Mat. Today Commun.* **24**, 100935 (2020)
46. Y. Pan, D. Pu, G. Liu, *Vacuum* **175**, 109291 (2020)
47. K.M. Hossain, M.Z. Hasan, *Mater. Today Commun.* (2020). <https://doi.org/10.1016/j.mtcomm.2020.101908>
48. Y.Q. Xu, S.Y. Wu, J.X. Guo, L.N. Wu, L. Peng, *J. Phys. Chem. Solids* **111**, 403 (2017)
49. I.R. Shein, V.L. Kozhevnikov, A.L. Ivanovskii, *Solid State Sci.* **10**, 217 (2008)
50. D. Ridgley, R. Ward, *J. Am. Chem. Soc.* **77**, 6132 (1955)
51. M.M. Rahaman, M.H.K. Rubel, M.A. Rashid, M.A. Alam, K.M. Hossain, M.I. Hossain, A.A. Khatun, M.M. Hossain, A.K.M.A. Islam, S. Kojima, N. Kumada, *J. Mater. Res. Technol.* **8**, 3783 (2019)
52. M.H.K. Rubel, M.M. Ali, M.S. Ali, R. Parvin, M.M. Rahaman, K.M. Hossain, M.I. Hossain, A.K.M.A. Islam, N. Kumada, *Solid State Commun.* **288**, 22 (2019)
53. S. Idrissi, H. Labrim, S. Ziti, L. Bahmad, *Appl. Phys. A* **126**, 190 (2020)
54. K.M. Hossain, S.K. Mitro, M.A. Hossain, J.K. Modak, M. Rasheduzzaman, M.Z. Hasan, *Mater. Today Commun.* (2020). <https://doi.org/10.1016/j.mtcomm.2020.101868>
55. K.M. Hossain, M.Z. Hasan, M.L. Ali, *Results Phys.* **19**, 103337 (2020)
56. M. Rasheduzzaman, K.M. Hossain, S.K. Mitro, M.A. Hadi, J.K. Modak, M.Z. Hasan, *Phys. Lett. A* **385**, 126967 (2021)
57. M. Born, K. Huang, M. Lax, *J. Phys.* **23**, 474 (1995)
58. S. Chaozhu, J. Long, S. Li, W. Yang, *J. Alloys Comp.* **650**, 553 (2015)
59. W. Voigt, *Lehrbuch Der Kristallphysik* (Taubner, Leipzig, 1928).
60. A. Reuss, *Z. Angew. Math. Mech.* **9**, 49 (1929)
61. R. Hill, *Proc. Phys. Soc. A* **65**, 349 (1952)
62. A.A. Maradudin, E.W. Montroll, G.H. Weiss, I.P. Ipatova, *Theory of Lattice Dynamics in the Harmonic Approximation* (Academic Press, New York, 1971).
63. M.A. Ali, M.M. Hossain, M.A. Hossain, M.T. Nasir, M.M. Uddin, M.Z. Hasan, *J. Alloy Comp.* **743**, 146 (2018)
64. S. Boucetta, *J. Magn. Alloys* **2**, 59 (2014)
65. S. Huang, R. Li, S.T. Qi, B. Chen, J. Shen, *Phys. Scr.* **89**, 065702 (2014)
66. I.N. Frantsevich, F.F. Voronov, S.A. Bokuta, *Elastic constants and elastic moduli of metals and insulators handbook* (Naukova Dumka, Kiev) 60–180 (1983)
67. M.I. Naher, S.H. Naqib, *J. Alloys Compd.* **829**, 54509 (2020)
68. Z. Sun, D. Music, R. Ahuja, J.M. Schneider, *Phys. Rev. B* **71**, 193402 (2005)
69. R. Majumder, S.K. Mitro, B. Bairagi, *J. Alloys Compd.* **836**, 155395 (2020)
70. S.K. Mitro, R. Mazumder, K.M. Hossain, M.Z. Hasan, M.E. Hossain, M.A. Hadi, *Chin. Phys. B* (2020). <https://doi.org/10.1088/1674-1056/abaf9d>
71. S.K. Mitro, K.M. Hossain, R. Majumder, M.Z. Hasan, *J. Alloys Compd.* **854**, 157088 (2021)
72. M. Zeng, R. Wang, B. Tang, L. Peng, W. Ding, *Model. Simul. Mater. Sci.* **20**, 035018 (2012)
73. U.F. Ozyar, E. Deligoz, K. Colakoglu, *Solid State Sci.* **40**, 92 (2015)
74. R. Gaillac, P. Pullumbi, F.X. Coudert, *J. Phys. Condens. Matter.* **28**, 275201 (2016)

Publisher's Note Springer Nature remains neutral with regard to jurisdictional claims in published maps and institutional affiliations.